Tunnel Magnetoresistance and Spin-Transfer-Torque Switching in Polycrystalline Co_2FeAl Full-Heusler-Alloy Magnetic Tunnel Junctions on Amorphous Si/SiO_2 Substrates

Zhenchao Wen, Hiroaki Sukegawa, Shinya Kasai, Koichiro Inomata, and Seiji Mitani

National Institute for Materials Science (NIMS), 1-2-1 Sengen, Tsukuba 305-0047, Japan

(Received 18 May 2014; revised manuscript received 25 July 2014; published 29 August 2014)

We study polycrystalline $B2$-type Co_2FeAl (CFA) full-Heusler-alloy-based magnetic tunnel junctions (MTJs) fabricated on a Si/SiO_2 amorphous substrate. Polycrystalline CFA films with a (001) orientation, a high $B2$ ordering, and a flat surface are achieved by using a MgO buffer layer. A tunnel magnetoresistance ratio up to 175% is obtained for a MTJ with a CFA/MgO/CoFe structure on a 7.5-nm-thick MgO buffer. Spin-transfer-torque-induced magnetization switching is achieved in the MTJs with a 2-nm-thick polycrystalline CFA film as a switching layer. By using a thermal activation model, the intrinsic critical current density (J_{c0}) is determined to be 8.2×10^6 A/cm^2, which is lower than 2.9×10^7 A/cm^2, the value for epitaxial CFA MTJs [Appl. Phys. Lett. **100**, 182403 (2012)]. We find that the Gilbert damping constant ($\boldsymbol{\alpha}$) evaluated by using ferromagnetic resonance measurements for the polycrystalline CFA film is approximately 0.015 and is almost independent of the CFA thickness (2–18 nm). The low $\boldsymbol{J_{c0}}$ for the polycrystalline MTJ is mainly attributed to the low $\boldsymbol{\alpha}$ of the CFA layer compared with the value in the epitaxial one (approximately 0.04).

DOI: 10.1103/PhysRevApplied.2.024009

I. INTRODUCTION

Half-metallic ferromagnets (HMFs) draw great interest because of the perfect spin polarization of conduction electrons at the Fermi level, which is considered to enhance the spin-dependent transport efficiency of high-performance spintronic devices [1–3]. Cobalt-based full Heusler alloys with the chemical formula Co_2YZ (where Y is a transition metal and Z is a main group element) are extensively studied as a type of HMFs owing to their high Curie temperature of approximately 1000 K, high spin polarization, and low damping constant [4,5]. They exhibit great potential for applications in spintronics, including current-perpendicular-to-plane giant magnetoresistance read heads [6,7], magnetoresistive random access memories (MRAMs) [8], and spin transistors such as spin-functional metal-oxide-semiconductor field-effect transistors (spin MOSFETs) [9,10]. In particular, magnetic tunnel junctions (MTJs) with Co-based full-Heusler-alloy electrodes have been shown tremendously increasing tunnel magnetoresistance (TMR) ratios during the past decade, since Inomata, Okamura, Goto, and Tezuka [11] demonstrated a TMR ratio of 16% by using $Co_2Cr_{0.6}Fe_{0.4}Al/AlO_x/CoFe$ MTJs at room temperature (RT) [12–21]. Recently, a remarkable TMR ratio of approximately 2000% at 4.2 K (354% at RT) was achieved by using epitaxial $Co_2MnSi/MgO/Co_2MnSi(001)$ MTJs, demonstrating the half-metallicity of Co-based Heusler alloys and a strong Δ_1 coherent tunneling effect in the MgO/Heusler MTJs [21].

The Co_2FeAl (CFA) alloy is of particular interest because of its high spin polarization (a half-metallic electronic structure) [22] and low effective damping constant $(\alpha) \sim 0.001$ [23], which are beneficial for enhancing the TMR ratio and lowering the magnetization switching current of spin-transfer torque (STT). CFA films prepared by using sputtering deposition generally have a disordered $B2$ structure (swapping between Y and Z sites) rather than an ordered $L2_1$ structure owing to the thermodynamic stability of CFA [24]. Nevertheless, the spin polarization calculated for the $L2_1$ structure is conserved even for the $B2$ structure [25]. Importantly, a CFA film with a (001) orientation has a large in-plane lattice spacing ($d_{(200)}/\sqrt{2} = d_{(110)} = 0.203$ nm) compared with other half-metallic Heusler alloys such as $Co_2FeAl_{0.5}Si_{0.5}$ ($d_{(110)} = 0.201$ nm) and Co_2MnSi ($d_{(110)} = 0.198$ nm). Therefore, a nearly perfect $CFA/MgO(001)$ heterostructure is easily achieved by the magnetron sputtering method, and this is favorable for enhancing the coherent tunneling effect [13,18]. Recently, TMR ratios as high as 360% at RT (785% at 10 K) were demonstrated in epitaxial CFA-based MTJs with a sputter-deposited MgO barrier [17–19]. The large TMR ratio originated from the high spin polarization of the CFA layer and the strong contribution of the coherent tunneling effect through Δ_1 Bloch states in the CFA and the MgO barrier. Moreover, (001)-textured CFA films can be grown on MgO-buffered Si/SiO_2 amorphous substrates, and a relatively large TMR ratio of 166% at RT (252% at 48 K) was achieved in a (001)-textured CFA/MgO/CoFe MTJ [20]. Such polycrystalline full-Heusler-alloy MTJs on amorphous substrates are desired because of their compatibility with practical industrial applications of full-Heusler-alloy spintronic devices, while single-crystal MgO(001) substrates have a limited scope of application.

Furthermore, STT-induced magnetization switching (STT switching), a key technology for writing information in spintronic devices, is realized by using MTJs with an epitaxial CFA ultrathin (approximately 1.5 nm) layer as a switching (free) layer [26]. However, a large critical switching current density (J_{c0}) of 2.9×10^7 A/cm^2 is observed owing to the enhancement of α, which is approximately 0.04, of the epitaxial CFA film. In addition, STT switching can be disturbed by the stabilization of intermediate magnetic states possibly because of the presence of in-plane magnetocrystalline anisotropy, which is generally seen in epitaxial magnetic films [e.g., fourfold anisotropy for cubic (001) films] [27]. Therefore, reducing the undesirable magnetic anisotropy by using polycrystalline Heusler-alloy films is effective for highly efficient STT switching.

In this work, we systematically study MTJs with (001)-textured polycrystalline CFA films on Si/SiO_2 amorphous substrates. A MgO buffer is introduced in the MTJs for achieving (001) texture with $B2$-ordering structure of CFA layers on the amorphous substrates. The (001) texture, $B2$ order, and surface morphology of the polycrystalline CFA films and also the TMR effect in the entire MTJ stacks are characterized for varying MgO buffer thickness. Furthermore, the MgO-barrier thickness and resistance-area product (RA) dependence of the TMR ratios are investigated for the polycrystalline CFA MTJs. STT switching is examined in low-RA MTJs with a thin polycrystalline CFA film (2.0 nm) as a free layer. J_{c0} of 8.2×10^6 A/cm^2 is demonstrated by a thermal activation model for switching current; this result is far lower than the value for epitaxial CFA MTJs [26]. The α values for the polycrystalline CFA films, obtained by using a waveguide-based ferromagnetic resonance (FMR) method, are almost constant against the CFA thickness, and a relatively low α of approximately 0.015 is demonstrated. We attribute the reduction in the J_{c0} of the STT switching to the reduced α of the polycrystalline CFA films.

II. EXPERIMENT

All multilayer stacks are deposited on thermally oxidized Si/SiO_2 amorphous substrates at RT by using an ultrahigh vacuum magnetron sputtering system with a base pressure lower than 4×10^{-7} Pa. MgO layers are deposited from a sintered MgO target by rf sputtering with an rf power density of 2.19 W/cm^2 and an Ar pressure of 10 mTorr. CFA layers are deposited from a stoichiometric $Co_{50}Fe_{25}Al_{25}$ (at. %) alloy target using dc power. The structural properties and surface morphology of CFA films on MgO buffers are characterized by out-of-plane (2θ–ω scan) x-ray diffraction (XRD) with Cu $K\alpha$ radiation ($\lambda = 0.15418$ nm) and atomic force microscopy (AFM), respectively. MTJ stacks with the structure of $CFA/MgO/Co_{75}Fe_{25}/IrMn/Ru$ (unit: nanometer) are deposited on MgO-buffered thermally oxidized Si/SiO_2 amorphous substrates and patterned into junctions with an active area of 5×10 μm^2 by conventional lithography methods with Ar ion milling. For STT switching, spin-valve MTJs with the structure of MgO (7.5)/Cr (40)/CFA (2)/MgO (0.6–0.8)/$Co_{75}Fe_{25}$ (5)/Ru (0.8)/$Co_{75}Fe_{25}$ (5)/IrMn (15)/Ta (5)/Ru (10) (unit: nanometer) are prepared on the amorphous substrates and nanofabricated into 100-nm-scaled ellipses. The actual areas of the MTJ nanopillars are obtained according to the ratio of the RA to the junction resistance; the RA is characterized by current-in-plane tunneling (CIPT) measurement [28] before patterning. The MTJ stacks are postannealed in a vacuum furnace for 30 min under a magnetic field of 5 kOe. The magnetotransport properties are measured by using a dc two- or four-probe method. The magnetic damping constant α of the polycrystalline CFA film is measured by waveguide-based FMR. The films are patterned into rectangular shape elements of 600×20 μm^2 by using UV lithography together with Ar ion milling, and then coplanar waveguides made of Au are fabricated on them. The FMR signal, obtained as change of the real part of the S_{21} signal, is determined by using a network analyzer. An external magnetic field along the longitudinal axis is varied from 0 to 1.9 kOe, while the excitation power is fixed as 0 dBm. All measurements are performed at RT.

III. RESULTS

A. Effect of MgO buffer on polycrystalline CFA films and TMR

Before MTJ multilayer films are grown, MgO buffer is deposited on a Si/SiO_2 amorphous substrate in order to establish the (001) texture of polycrystalline CFA films by taking advantage of the unique (001)-texture property of MgO layers on an amorphous substrate. CFA films are subsequently grown on the MgO buffer layer, and the structural properties of the CFA films depending on the MgO buffer thickness are investigated by XRD. The out-of-plane XRD patterns of 30-nm-thick CFA films are shown in Fig. 1(a); the CFA films are annealed at $T_a = 400$ °C, and the thicknesses of the MgO buffers (t_{MgO}) are 2.5, 5.0, 7.5, and 10.0 nm. In addition to the peaks (denoted by "s") from Si/SiO_2 substrates, MgO(002), CFA(002), and (004) peaks are observed along with the absence of other oriented peaks, demonstrating the (001) texture established in the stacks. Figure 1(b) shows the t_{MgO} dependence of the integrated intensity of CFA(002) peaks for as-deposited CFA films and CFA films annealed at 400 °C and 480 °C. With increasing t_{MgO}, the intensity of the peaks initially increases for all samples owing to the improved (001) texture of the MgO buffer layer, reaching a maximum at $t_{MgO} = 7.5$ nm. The reduction in intensity at $t_{MgO} =$ 10 nm may be caused by the degraded surface morphology of the MgO buffer layer. In addition, the XRD intensity

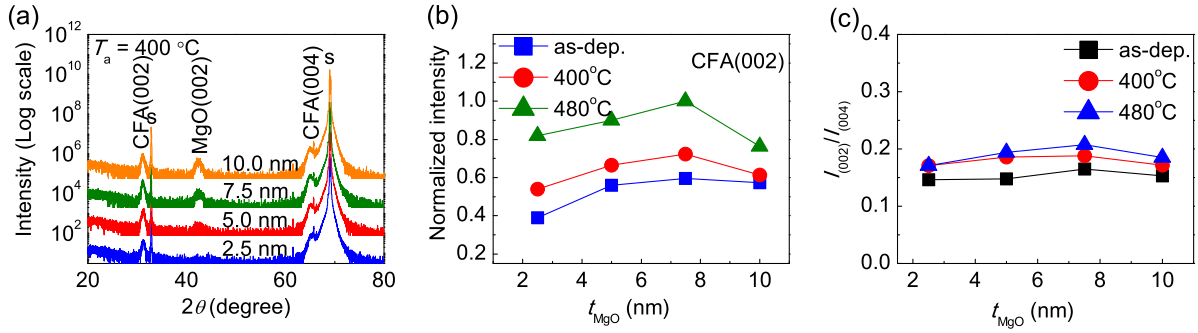

FIG. 1. (a) Out-of-plane (2θ–ω scan) XRD patterns for polycrystalline CFA full-Heusler-alloy films on MgO-buffered Si/SiO_2 amorphous substrates with varied MgO buffer thickness t_{MgO}: 2.5, 5.0, 7.5, and 10.0 nm. (b) Normalized integrated intensity of the CFA(002) peak and (c) ratios of (002) to (004) peaks as a function of t_{MgO} for as-deposited (as-dep.) samples and those annealed at 400 °C and 480 °C.

increases with increasing annealing temperature, which indicates that the increasing temperature improves the $B2$ order and (001) texture of the CFA films. In the XRD 2θ–ω scan with the diffraction vector along CFA[111], (111) reflection is not detected, indicating that the CFA films have a $B2$-ordering structure with swapping between Fe and Al atoms while Co atoms occupy the regular sites. The degree of $B2$ ordering is estimated according to the ratio of the integrated intensity of the CFA(002) and (004) peaks. The peaks are fitted by Voigt profiles, and the ratio of their integrated intensities, i.e., the ratio of $I(002)$ to $I(004)$, is shown in Fig. 1(c). The maximum $I(002)/I(004)$ value is obtained at $t_{MgO} = 7.5$ nm for all of the samples: as-deposited and annealed at 400 °C or 480 °C. This value is comparatively large for CFA films annealed at 480 °C, indicating the improvement of the $B2$ ordering and the mosaicity of the CFA films due to annealing at high temperature. The degree of $B2$ ordering, S_{B2}, can be evaluated by using the ratios according to the following equation [29]:

$$S_{B2} = \sqrt{\frac{[I(002)/I(004)]_{expt}}{[I(002)/I(004)]_{calc}}}, \qquad (1)$$

where $[I(002)/I(004)]_{expt}$ is the ratio of the integrated intensity of the (002) peak to that of the (004) peak as determined by experiments and $[I(002)/I(004)]_{calc}$ is the ideal ratio of the two peaks. For $t_{MgO} = 7.5$ nm, the ordering parameter S_{B2} is calculated to be 0.89, 0.95, and 0.98 for CFA films as deposited and annealed at 400 °C and 480 °C, respectively. The results demonstrate that a high $B2$ order and an excellent (001) texture are established in the polycrystalline CFA films on MgO-buffered Si/SiO_2 amorphous substrates.

For stacking MTJ multilayers with the polycrystalline CFA films, the t_{MgO} dependence of the surface morphology of the CFA films is investigated. Figure 2 shows the average surface roughness (R_a) and peak-to-valley (P-V) value as a function of t_{MgO} for 30-nm-thick CFA films annealed at 400 °C and 480 °C, respectively. For the samples annealed at 400 °C, flat surfaces with $R_a \sim 0.1$ nm and P-V ranging from 1.3 to 1.5 nm are observed for all values of t_{MgO}. The inset in Fig. 2 shows an example of AFM images of the samples (annealed at 400 °C on a 7.5-nm-thick MgO buffer). The results indicate the feasibility of stacking MTJs with a thin MgO barrier. In addition, the samples annealed at 480 °C with higher R_a and P-V values are observed as well as a large t_{MgO} dependence.

The whole MTJ stacks with the structure of MgO (t_{MgO})/CFA (30)/MgO (t_{barr})/$Co_{75}Fe_{25}$ (5)/IrMn (15)/Ru (10) (unit: nanometer) are then fabricated on Si/SiO_2 substrates with varying MgO buffer thickness t_{MgO} (2.5–10.0 nm) and MgO barrier thickness t_{barr} (1.5, 1.8, and 2.0 nm). The stacks are annealed at 370 °C in the presence of a magnetic field of 5 kOe. Figure 3 shows TMR ratios as a function of t_{MgO} for the polycrystalline CFA MTJs measured at RT by using CIPT. The 30-nm-thick CFA

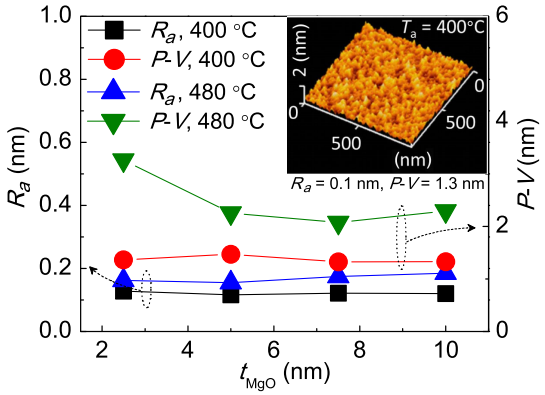

FIG. 2. Surface morphology of polycrystalline CFA full-Heusler-alloy films on MgO-buffered Si/SiO_2 amorphous substrates with respect to the thickness of the MgO buffer. The CFA films are 30 nm thick and are deposited at RT and postannealed at 400 °C and 480 °C, respectively. Inset: AFM image of the surface of the CFA film annealed at 400 °C.

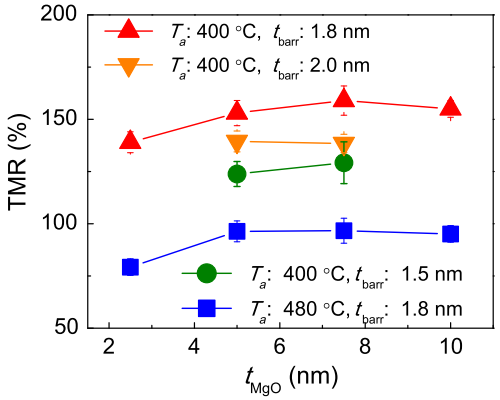

FIG. 3. TMR ratios as a function of MgO buffer thickness t_{MgO} for polycrystalline CFA/MgO/CoFe MTJs with different thicknesses of the MgO barrier t_{barr}: 1.5, 1.8, and 2.0 nm. The 30-nm-thick CFA bottom electrodes are directly deposited on the MgO buffer layer and postannealed at 400 °C and 480 °C after deposition at RT. The MTJ stacks are annealed at 370 °C before the CIPT measurement.

films are postannealed at $T_a = 400$ °C and 480 °C in order to improve the $B2$ ordering. The TMR ratios obtained in MTJs with $T_a = 400$ °C are higher than those of MTJs with $T_a = 480$ °C, which can be attributed to a better CFA/MgO-barrier interface due to the flat CFA surface annealed at 400 °C, although a higher degree of $B2$ ordering is observed for $T_a = 480$ °C, as shown in Figs. 1 and 2. With increasing t_{MgO}, the TMR ratio increases and is nearly saturated at $t_{MgO} > 5$ nm, indicating that high-quality CFA films with $B2$ order and (001) texture are established with the more-than-5-nm-thick MgO buffer layer, which is consistent with the XRD analyses. A slight reduction in the TMR ratio is observed at $t_{MgO} = 10$ nm, which could be caused by the reduction in the degree of (001) orientation of the MgO buffer. The MTJs with a 1.8-nm-thick MgO barrier exhibit larger TMR ratios than those with 1.5-and 2.0-nm-thick MgO barriers, which could be due to the plastic relaxation of the MgO barrier [30] and/or the oscillatory behavior of the TMR ratio as a function of MgO thickness [18].

B. MgO barrier thickness and *RA* dependences of TMR

In order to realize STT switching in the polycrystalline CFA MTJs, it is expected that introduction of a conductive underlayer, reduction in the free-layer thickness, and control of the *RA* of the barrier layer are required. The MgO barrier thickness and *RA* dependences of the TMR ratio are investigated by using spin-valve MTJs with the structure of MgO buffer (7.5)/Cr (40)/CFA (30)/MgO (t_{barr}: 1.2–2.0)/$Co_{75}Fe_{25}$ (5)/IrMn (15)/Ta (5)/Ru (10) (unit: nanometer) on a Si/SiO_2 substrate. A Cr underlayer is selected as the conductive electrode because Cr has a very small lattice mismatch with CFA (approximately 0.6%) and can further facilitate the ordering structure of full Heusler alloys [13]. The Cr layers for the samples as deposited and annealed at 400 °C and 600 °C are prepared on the 7.5-nm-thick MgO buffer for the MTJ stacks. The entire stacks are annealed at 370 °C in the presence of a magnetic field of 5 kOe, and then their TMR ratios and *RA* values are characterized by using CIPT measurement.

Figure 4(a) shows the dependence of the TMR ratios on the nominal thickness of the MgO barrier t_{barr} for the MTJs with different Cr annealing conditions. For the samples that are as deposited and annealed at 400 °C, the TMR ratio increases with t_{barr}, and TMR ratios greater than 100% are achieved for the whole range of t_{barr}. This result means that the (001) texture and $B2$ ordering of CFA films can be maintained on the MgO/Cr buffer layers. We obtain the largest TMR ratio of 175% for the 400 °C annealed sample with $t_{barr} = 1.95$ nm; this TMR ratio is higher than 166%, which is observed in the MTJ without the Cr buffer, which indicates that the Cr buffer with optimal conditions promotes CFA(001) growth and improves the effective tunneling spin polarization. On the other hand, the samples annealed at a high temperature (600 °C) exhibit smaller TMR ratios (80%–120%). This difference is attributed to the rough surface ($R_a = 0.4$ nm and P-$V = 3.2$ nm) of the

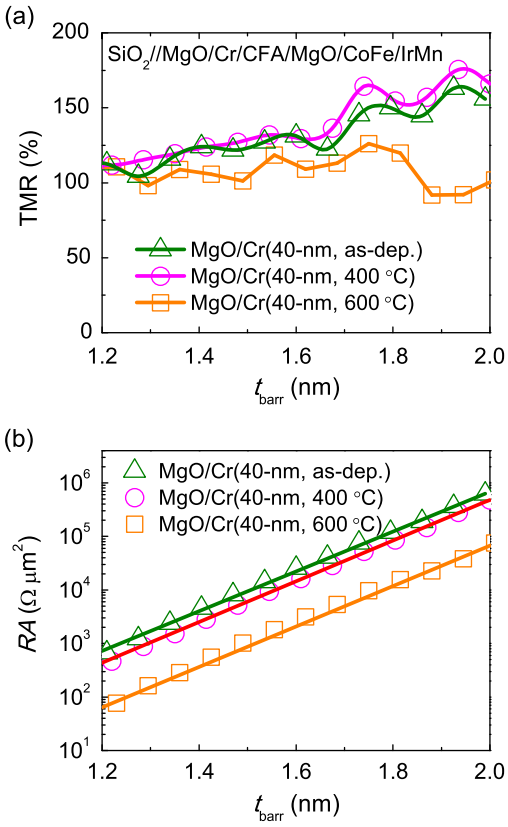

FIG. 4. The thickness of MgO barrier, t_{barr}, dependence of (a) TMR ratios and (b) *RA* at RT for polycrystalline CFA/MgO/CoFe MTJs with as-deposited, 400 °C and 600 °C annealed MgO(7.5 nm)/Cr(40 nm) buffer layers on SiO_2 amorphous substrates, characterized by using CIPT measurement.

CFA film on the Cr layer annealed at 600 °C, which can lead to a declined crystalline orientation of the MgO(001) barrier. Furthermore, oscillation behavior of the TMR ratios as a function of t_{barr} is observed for all of the structures. The TMR oscillation behavior is typically observed in epitaxial MTJs such as Fe/MgO/Fe [31], Co_2MnSi/MgO/Co_2MnSi [32], $Co_2Cr_{0.6}Fe_{0.4}Al$/MgO/$Co_2Cr_{0.6}Fe_{0.4}Al$ [33], and CFA/MgO/CoFe [18] MTJs, while it is absent in polycrystalline MTJs such as CoFeB/MgO/CoFeB [34] MTJs. More remarkable oscillation amplitude in epitaxial full-Heusler-alloy-based MTJs than that of epitaxial Fe/MgO/Fe MTJs is observed, which may be related to the electronic structures of full-Heusler-alloy electrodes and the full-Heusler-alloy/MgO interface; however, the origin is not understood yet. The unexpected oscillation behavior in the polycrystalline CFA MTJs may be also attributed to the unique electronic structure of CFA and the interface. In addition, the flat buffer layer with a good crystallinity enables us to achieve a well-defined layer-by-layer growth for the CFA layer and the MgO barrier, which may be advantageous for observing the oscillatory behavior. The oscillation period is approximately 0.2 nm in nominal thickness, which seems to be shorter than that for the epitaxial CFA/MgO/CoFe (0.32 nm, short-period) [18]. Further investigation is needed to clarify the origin of the behavior.

The *RA* as a function of the MgO barrier thickness is plotted in Fig. 4(b). We observe a typical behavior of an exponential increase with increasing t_{barr}. According to the Wenzel-Kramer-Brillouin approximation, the relationship between *RA* and t_{barr} can be expressed as follows:

$$RA(t_{barr}) \propto \exp\left(\frac{4\pi\sqrt{2m\phi}}{h} t_{barr}\right), \qquad (2)$$

where h, m, and ϕ are Planck's constant, the effective electron mass assumed as a free electron mass (9.11×10^{-31} kg) here, and the barrier height energy of the tunnel barrier, respectively [31]. A similar barrier height of 0.7 eV is obtained for all three samples by the fitting of *RA*-t_{barr} curves. This value is greater than the reported values for Fe/MgO/Fe grown by using molecular-beam-epitaxy (0.39 eV) [31], sputtered CoFeB/MgO/CoFeB (0.29–0.39 eV) [35–37], and CoFeB/MgO (electron-beam evaporated)/CoFeB (0.48 eV) [38] MTJs. The reasons may be due to the different densities of oxygen vacancy defects in the MgO barriers and/or the deviation of the actual MgO thickness from the nominal one.

Figure 5 shows TMR ratios in a low-*RA* regime for the polycrystalline CFA MTJs with 2-nm-thick CFA film as a free layer. The MTJs are annealed at 225 °C for 30 min in order to reduce the influence of the Cr layer to CFA. A TMR ratio of 40%–60% is achieved with an *RA* of 7–20 Ω μm^2 (nominal MgO thickness: 0.6–0.8 nm) for the 100-nm-scaled elliptical MTJs with the thin CFA layer,

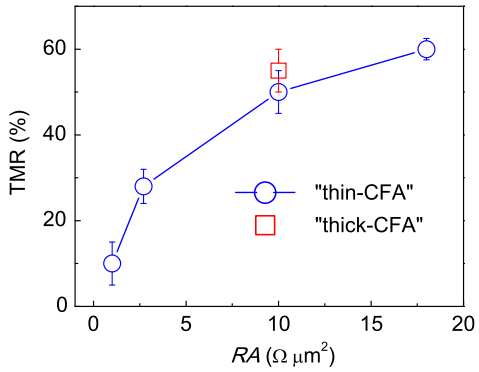

FIG. 5. *RA* dependence of TMR ratios for polycrystalline CFA MTJs with a 2-nm-thick CFA layer ("thin-CFA") as a bottom electrode. The squared symbol indicates the TMR ratio for a polycrystalline CFA MTJ with a 30-nm-thick CFA layer ("thick-CFA").

which is favorable for achieving STT switching in the MTJ stacks with a thin CFA free layer and the low *RA* value. In addition, the TMR ratio of the polycrystalline MTJs with 2-nm-thick CFA film is comparable to that with a thick (30-nm) CFA film at a low *RA* value, as shown in Fig. 5, which indicates that the (001) texture and *B*2 ordering can be maintained in the thin 2-nm-thick CFA films.

C. STT-induced magnetization switching

STT-induced magnetization switching is performed in spin-valve MTJs with the structure of Si/SiO_2-substrate/MgO (7.5)/Cr (40)/CFA (2)/MgO (0.6–0.8)/$Co_{75}Fe_{25}$ (5)/Ru (0.8)/$Co_{75}Fe_{25}$ (5)/IrMn (15)/Ta (5)/Ru (10) (unit: nanometer). A schematic of the structure of a polycrystalline CFA MTJ nanopillar is shown in Fig. 6(a). The synthetic antiferromagnetic coupling exchange bias of CoFe/Ru/CoFe/IrMn is employed to reduce the offset magnetic field of hysteresis loops. Figure 6(b) indicates the tunneling resistance of a MTJ nanopillar as a function of the applied magnetic field (H) measured with a dc bias voltage of 1 mV. A TMR ratio of 43% is observed in the MTJ with a thin CFA free layer (2.0 nm) and MgO barrier (0.75 nm). Sharp switching between parallel (P) and antiparallel (AP) magnetic configurations is observed. The *RA* of the MTJ is determined by using CIPT measurements to be 13 Ω μm^2, and the active area of the MTJ nanopillar is calculated to be 1.24×10^{-2} μm^2. The hysteresis offset field (H_{offset}) and the coercivity field (H_c) are determined by using the *R*-*H* loops to be −11 and 26 Oe, respectively. Figure 6(c) shows the representative resistance-current (*R*-*I*) loops of the CFA MTJ nanopillar measured by a dc current with a sweep rate of 1.2×10^{-4} A/s at different magnetic fields of 0, −11, and −20 Oe, respectively. The positive current indicates that electrons flow from the bottom electrode to the top electrode. Magnetic switching between P (low-resistance)

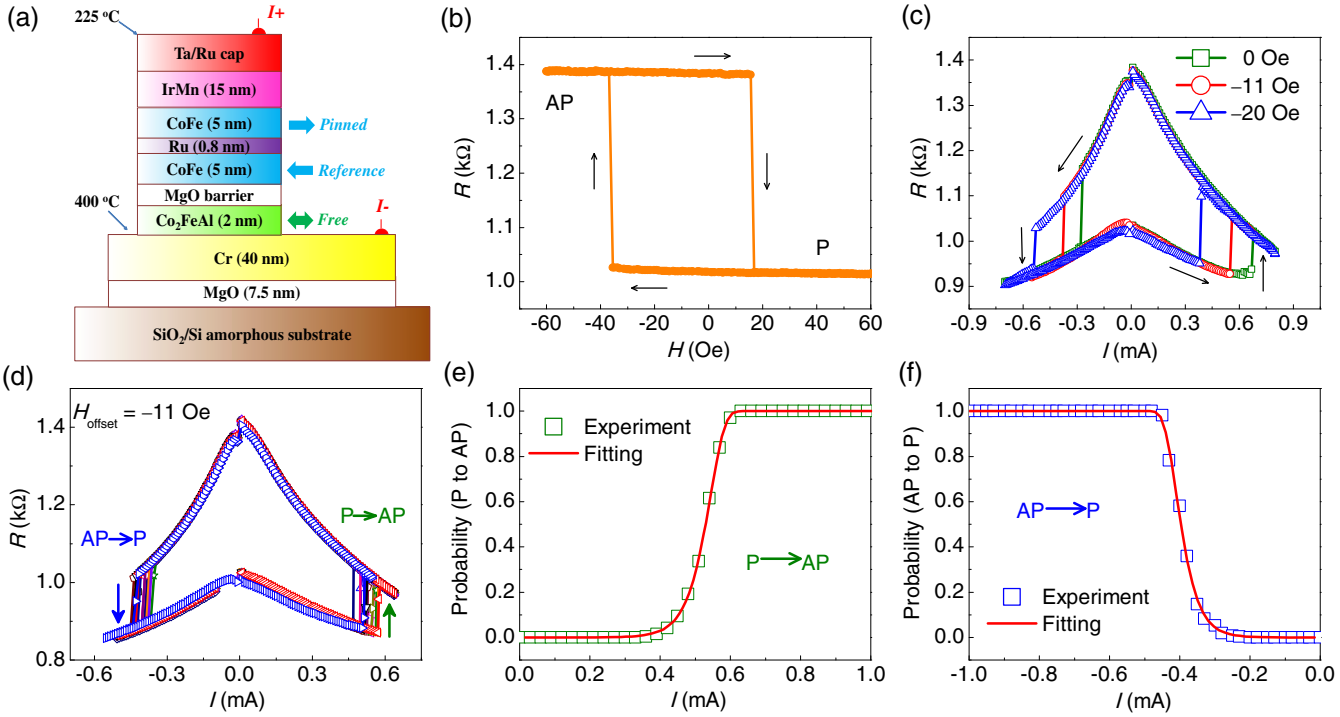

FIG. 6. (a) Schematic illustration of the structure of a polycrystalline CFA MTJ nanopillar. (b) *R-H* loops for a polycrystalline CFA MTJ nanopillar. Wide arrows show the magnetic configurations of bottom (free) and top (reference) electrodes of the MTJ, and narrow arrows indicate the sweep direction of the applied magnetic field. (c) *R-I* loops for the MTJ at magnetic fields of 0, −11, and −20 Oe, respectively. Arrows indicate the sweep direction of the applied current. (d) Representative *R-I* loops of the CFA MTJ at an applied magnetic field of −11 Oe. (e),(f) Switching probabilities for $I_{c,\mathrm{P}->\mathrm{AP}}$ and $I_{c,\mathrm{AP}->\mathrm{P}}$ obtained by repeating *R-I* measurements for 300 times. Solid lines are fitting curves given by Eq. (3). All measurements are performed at RT.

and AP (high-resistance) states is achieved owing to the current. When current is applied in the negative (positive) direction, the P (AP) state can be obtained from the AP (P) state, corresponding to magnetization reversal of the CFA free layer. Also, the critical switching currents (I_c) in both directions shift in the negative direction with the decrease of the magnetic field from 0 to −20 Oe. These results indicate typical behaviors of STT-induced magnetization switching.

Since the STT switching by the dc current is a thermally activated process [39–41], we use a thermal activation model for switching currents deduced from *R-I* loops to evaluate the intrinsic critical switching current density (J_{c0}) and thermal stability factor Δ_0 ($=K_uV/k_BT$) for the MTJ, where K_u is the uniaxial magnetic anisotropy, V is the volume of the free layer, k_B is the Boltzmann constant, and T is the absolute temperature. In the thermal activation model, the sweep current $I(t)$ is assumed to increase linearly with time t, i.e., $I(t) = vt$, and the cumulative probability distribution function $P(t)$ of the switching current in H_{offset} can be expressed as

$$P(t) = 1 - \exp\left(-\frac{f_0 I_{c0}}{v\Delta_0} \left\{ \exp\left[-\Delta_0 \left(1 - \frac{vt}{I_{c0}} \right) \right] - \exp[-\Delta_0] \right\} \right), \tag{3}$$

where f_0 is the effective attempt frequency ($=10^9$ Hz), I_{c0} is the intrinsic switching current, and v is a constant sweep rate of the sweep current in the measurement of *R-I* loops [41]. The distribution of the critical switching current I_c is obtained by repeating the measurement of the *R-I* loops for 300 times. Figure 6(d) shows typical *R-I* loops at $H_{\mathrm{offset}} = -11$ Oe for the polycrystalline CFA MTJ nanopillar. The mean critical currents in the positive ($I_{c,\mathrm{P}\to\mathrm{AP}}$) and negative ($I_{c,\mathrm{AP}\to\mathrm{P}}$) directions are determined to be 530 and 400 μA, corresponding to the critical current density of 4.3×10^6 ($J_{c,\mathrm{P}\to\mathrm{AP}}$) and 3.2×10^6 A/cm^2 ($J_{c,\mathrm{AP}\to\mathrm{P}}$), respectively. Figures 6(e) and 6(f) show the switching probability for $I_{c,\mathrm{P}\to\mathrm{AP}}$ and $I_{c,\mathrm{AP}\to\mathrm{P}}$ as a function of the sweep current. By using the constant sweep rate $v = 1.2 \times 10^{-4}$ A/s in the measurement of *R-I* loops, the switching probability is fitted by using Eq. (3), as shown by the solid lines. As a result, the intrinsic current density of $J_{c0,\mathrm{P}\to\mathrm{AP}}$ ($J_{c0,\mathrm{AP}\to\mathrm{P}}$) $= 9.1 \times 10^6$ A/cm^2

$(7.3 \times 10^6\ \mathrm{A/cm^2})$ and thermal stability of $\Delta_{0,\mathrm{P}\to\mathrm{AP}}$ $(\Delta_{0,\mathrm{AP}\to\mathrm{P}}) = 30.0\ (28.4)$ are achieved for the polycrystalline CFA MTJ nanopillar.

D. Gilbert damping of the polycrystalline CFA film

The Gilbert damping parameter α is a critical parameter for determining the critical current density of STT switching. In order to examine α for the polycrystalline CFA film, waveguide-based FMR is performed in a single ferromagnetic layered sample, consisting of SiO_2-substrate// MgO(7.5 nm)/Cr(40 nm)/CFA(2–18 nm) structure. Typical FMR spectra with varied external magnetic fields (H_{ext}) for a sample of 18-nm-thick CFA are shown in the inset in Fig. 7(a). A clear shift in the resonant frequency can be seen as H_{ext} increases from 500 to 1500 Oe. The peak intensity is relatively small at low magnetic field, possibly because of the anisotropy distribution inside the film.

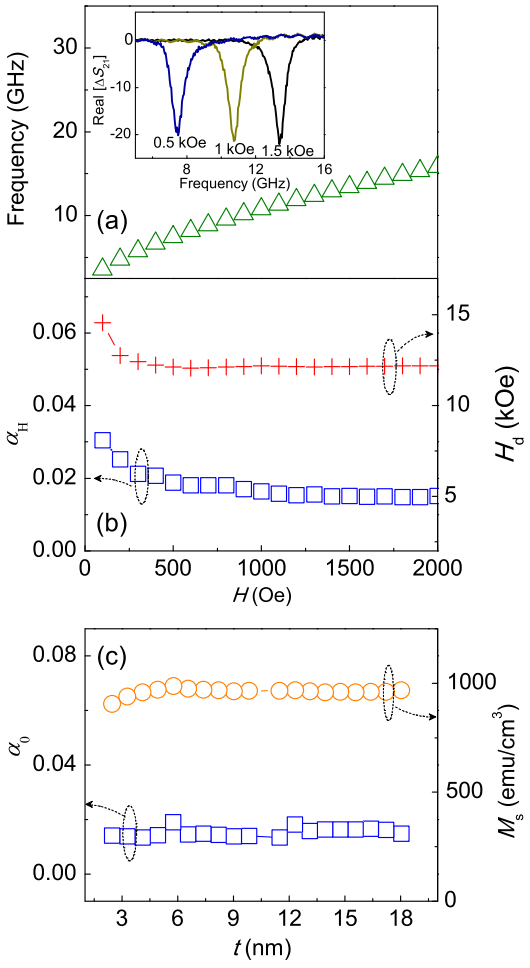

FIG. 7. The H_{ext} dependence of (a) resonant frequency f_0, (b) demagnetization field H_d, and magnetic damping parameter α_H estimated by fitting the FMR spectrum at each magnetic field for a sample of an 18-nm-thick polycrystalline CFA film. The inset in (a) is typical FMR spectra at H_{ext} of 500, 1000, and 1500 Oe. (c) CFA thickness t dependence of saturation magnetization M_s and damping constant α_0 of the polycrystalline CFA film.

Figures 7(a) and 7(b) show the H_{ext} dependence of the resonant frequency (f_0), demagnetization field (H_d), and magnetic damping parameter (α_H), respectively, estimated by fitting each spectrum by using an analytical solution [42]. Here, we assume the gyromagnetic ratio (γ) as $2\pi \times 0.00297$ GHz/Oe and neglect the in-plane magnetic anisotropic field. Both H_d and α_H exhibit a weak dependence on H_{ext} possibly due to the anisotropy distribution, which becomes saturated at a high-magnetic-field range. The f_0 is fitted by using the simplified Kittel formula:

$$f_0 = \frac{\gamma}{2\pi}\sqrt{H_{\mathrm{ext}}(H_{\mathrm{ext}} + H_d)}. \tag{4}$$

Then, we obtain $H_d = 12154 \pm 17.9$ Oe, which agrees well with the values obtained in the individual resonant spectrum for $H_{\mathrm{ext}} > 300$ Oe. The magnetic field dependence of α can be excluded by the fitting equation

$$\alpha_H = \alpha + k\exp(-H_{\mathrm{ext}}/H_0), \tag{5}$$

where k and H_0 are fitting parameters and α is estimated to be 0.0148 ± 0.0003. Figure 7(c) summarizes the CFA thickness dependence of the saturation magnetization M_s and Gilbert damping constant α of polycrystalline CFA films. The weak thickness dependence of M_s and α indicates that the CFA film guarantees a good quality even in a thin thickness regime at around 2 nm.

IV. DISCUSSION

By using polycrystalline CFA full-Heusler-alloy thin films, MTJs with the structure of CFA/MgO/$Co_{75}Fe_{25}$ are successfully fabricated on a Si/SiO_2 amorphous substrate. The effects of the MgO buffer on the structural properties of the polycrystalline CFA films and the TMR in the MTJs are investigated. Optimized (001) texture, $B2$ order, and surface morphology of the CFA films is demonstrated on a 7.5-nm-thick MgO buffer, which contributes a large TMR ratio in the whole polycrystalline MTJ stacks. In order to achieve STT switching, Cr underlayers are utilized as a conductive electrode on the optimized MgO buffer. The Cr layer is known to have very small lattice mismatch (approximately 0.6%) with CFA and facilitate the ordering structure of full Heusler alloys. A TMR ratio of 175% is achieved in the polycrystalline CFA MTJs on a MgO/Cr-buffered Si/SiO_2 substrate. The buffer layer dependence of the structural properties of polycrystalline CFA films and the TMR ratios in entire MTJ stacks are significant for practical spintronic applications of full-Heusler-alloy materials. A proper buffer layer with minimal diffusion and enhanced (001) texture and ordering parameter of polycrystalline full Heusler alloys is required for further increasing the TMR ratios of the MTJs.

STT switching is performed in the CFA MTJs with polycrystalline CFA as a free layer. The average intrinsic current density $J_{c0} = (J_{c0,P\to AP} + J_{c0,AP\to P})/2 = 8.2 \times 10^6$ A/cm^2 for the polycrystalline CFA MTJ is generally comparable to that reported for CoFeB MTJs with in-plane magnetization [43,44]; however, it is much lower than the value of 2.9×10^7 A/cm^2 for epitaxial CFA MTJs [26]. Based on Slonczewski's model of STT switching [45,46], the simplified J_{c0}, ignoring external magnetic fields, is given by

$$J_{c0} = \left(\frac{2e}{\hbar}\right)\frac{\alpha M_s t}{\eta} H_{\text{eff}}, \tag{6}$$

where e is the electron charge, $\hbar$ is the reduced Planck's constant, M_s is the saturation magnetization, t is the thickness of the free layer, η is the spin-transfer efficiency, and H_{eff} is the effective field acting on the free layer, including the magnetocrystalline anisotropy field, demagnetization field, and stray field. The polycrystalline CFA free layer ($t = 2.0$ nm) is thicker than the epitaxial one ($t = 1.5$ nm). A similar M_s (approximately 1000 emu/cm^3) at RT is observed for both polycrystalline and epitaxial CFA films. The η of the polycrystalline CFA MTJs should be smaller than that of the epitaxial CFA MTJs, because the TMR ratio of the polycrystalline CFA MTJs (43%) is lower than that of the epitaxial CFA MTJs (60%) [26]. Accordingly, the low J_{c0} in the polycrystalline CFA MTJs can be mainly attributed to the small α of the polycrystalline CFA free layer (approximately 0.015) compared with that of the epitaxial CFA films (approximately 0.04) [26]. For the polycrystalline CFA MTJs, annealing is performed with a low temperature of 225 °C and a short time of 30 min, whereas the epitaxial CFA MTJs are annealed at 360 °C for 1 h; this annealing condition could be a factor in the reduction in α [47]. As a result, a lower J_{c0} is obtained in the polycrystalline CFA MTJs than that in the epitaxial ones. However, the α value is still greater than that reported for a 50-nm-thick CFA film on a MgO layer annealed at 600 °C (approximately 0.001) [23]; this discrepancy may be attributed to the interdiffusion of Cr atoms into the CFA layer and the residual magnetic moments on the Cr surface. Consequently, a proper buffer material is strongly required for CFA full-Heusler-alloy MTJs in order to reduce the α of the free layer and thus the J_{c0} of STT switching. Another factor for reducing J_{c0} is the magnetic anisotropy of the free layer. In perpendicular anisotropy CoFeB/MgO/CoFeB tunnel junctions, a low-current density for STT switching is demonstrated owing to the perpendicular magnetic anisotropy (PMA) [48–53]. To evaluate the contribution of interface PMA, magnetization measurements at in-plane and out-of-plane of the polycrystalline CFA film are performed. An effective anisotropy energy density (K_{eff}) of -5×10^6 erg/cm^3 is obtained for a 2-nm-thick CFA/MgO structure, where the negative K_{eff} indicates the CFA layer is in-plane magnetized. In general, K_{eff} can be simply expressed by the equation $K_{\text{eff}} = K_v + K_i/t$, where K_v is the volume anisotropy energy density which can be treated as the demagnetization energy density ($2\pi M_s^2$) for simplicity, K_i is the interface anisotropy energy density, and t is the thickness of the CFA layer. As a result, the value of K_i can be calculated to be 0.25 erg/cm^2, indicating that an interface PMA is induced at the CFA/MgO interface. In the CFA/MgO MTJs, the interface PMA can cause a reduced effective anisotropy and may also play a role for the reduction in J_{c0}. For further decreasing J_{c0}, a chosen buffer material, out-of-plane magnetization of the CFA free layer [54–56], and/or advanced fabricating techniques for high-quality CFA MTJs are required.

V. CONCLUSION

In conclusion, TMR ratios and STT-induced magnetization switching are studied in (001)-textured polycrystalline CFA full-Heusler-alloy-based MTJs on Si/SiO$_2$ amorphous substrates. CFA films with a good (001) texture and high $B2$ order are achieved on MgO-buffered Si/SiO$_2$ amorphous substrates. The MgO barrier thickness and RA dependences of the TMR ratio in the polycrystalline CFA MTJs are also studied. Moreover, STT switching is achieved in the MTJs with a thin polycrystalline CFA film (2.0 nm) as a free layer. The J_{c0} of 8.2×10^6 A/cm^2 is demonstrated for the polycrystalline CFA MTJs with in-plane magnetization using a thermal activation model for a cumulative switching probability distribution with a sweep current. The J_{c0} is much lower than that reported for epitaxial CFA MTJs, which is mainly attributed to the reduced α of the polycrystalline CFA free layer.

ACKNOWLEDGMENTS

This work is partly supported by the Japan Science and Technology Agency, CREST, and JSPS KAKENHI Grant No. 23246006.

[1] R. A. de Groot, F. M. Mueller, P. G. vanEngen, and K. H. J. Buschow, New class of materials: Half-metallic ferromagnets, Phys. Rev. Lett. **50**, 2024 (1983).

[2] C. Felser, G. H. Fecher, and B. Balke, Spintronics: A challenge for materials science and solid-state chemistry, Angew. Chem., Int. Ed. **46**, 668 (2007).

[3] T. Graf, C. Felser, and S. S. P. Parkin, Simple rules for the understanding of Heusler compounds, Prog. Solid State Chem. **39**, 1 (2011).

[4] I. Galanakis, P. Dederichs, and N. Papanikolaou, Slater-Pauling behavior and origin of the half-metallicity of the full-Heusler alloys, Phys. Rev. B **66**, 174429 (2002).

[5] M. Oogane, T. Kubota, Y. Kota, S. Mizukami, H. Naganuma, A. Sakuma, and Y. Ando, Gilbert magnetic damping constant of epitaxially grown Co-based

Heusler alloy thin films, Appl. Phys. Lett. **96**, 252501 (2010).

[6] T. Furubayashi, K. Kodama, H. Sukegawa, Y. K. Takahashi, K. Inomata, and K. Hono, Current-perpendicular-to-plane giant magnetoresistance in spin-valve structures using epitaxial $Co_2FeAl_{0.5}Si_{0.5}/Ag/Co_2FeAl_{0.5}Si_{0.5}$ trilayers, Appl. Phys. Lett. **93**, 122507 (2008).

[7] Y. Sakuraba, K. Izumi, T. Iwase, S. Bosu, K. Saito, K. Takanashi, Y. Miura, K. Futatsukawa, K. Abe, and M. Shirai, Mechanism of large magnetoresistance in $Co_2MnSi/Ag/Co_2MnSi$ devices with current perpendicular to the plane, Phys. Rev. B **82**, 094444 (2010).

[8] Z. Bai, L. Shen, G. Han, and Y. P. Feng, Data storage: Review of Heusler compounds, SPIN **02**, 1230006 (2012).

[9] Y. Shuto, R. Nakane, W. Wang, H. Sukegawa, S. Yamamoto, M. Tanaka, K. Inomata, and S. Sugahara, A new spin-functional metal–oxide–semiconductor field-effect transistor based on magnetic tunnel junction technology: Pseudo-Spin-MOSFET, Appl. Phys. Express **3**, 013003 (2010).

[10] Y. Shuto, S. Yamamoto, H. Sukegawa, Z. C Wen, R. Nakane, S. Mitani, M. Tanaka, K. Inomata, and S. Sugahara, Design and performance of pseudo-spin-MOSFETs using nano-CMOS devices, in *Proceedings of the 2012 IEEE International Electron Devices Meeting (IEDM)* (IEEE, New York, 2012), pp. 29.6.1–29.6.4 [http://ieeexplore.ieee.org/xpl/articleDetails.jsp?arnumber=6479131].

[11] K. Inomata, S. Okamura, R. Goto, and N. Tezuka, Large tunneling magnetoresistance at room temperature using a Heusler alloy with the B2 structure, Jpn. J. Appl. Phys. **42**, L419 (2003).

[12] S. Tsunegi, Y. Sakuraba, M. Oogane, K. Takanashi, and Yasuo Ando, Large tunnel magnetoresistance in magnetic tunnel junctions using a Co_2MnSi Heusler alloy electrode and a MgO barrier, Appl. Phys. Lett. **93**, 112506 (2008).

[13] H. Sukegawa, W. H. Wang, R. Shan, T. Nakatani, K. Inomata, and K. Hono, Spin-polarized tunneling spectroscopy of fully epitaxial magnetic tunnel junctions using $Co_2FeAl_{0.5}Si_{0.5}$ Heusler alloy electrodes, Phys. Rev. B **79**, 184418 (2009).

[14] R. Shan, H. Sukegawa, W. H. Wang, M. Kodzuka, T. Furubayashi, T. Ohkubo, S. Mitani, K. Inomata, and K. Hono, Demonstration of half-metallicity in Fermi-level-tuned Heusler alloy $Co_2FeAl_{0.5}Si_{0.5}$ at room temperature, Phys. Rev. Lett. **102**, 246601 (2009).

[15] N. Tezuka, N. Ikeda, F. Mitsuhashi, and S. Sugimoto, Improved tunnel magnetoresistance of magnetic tunnel junctions with Heusler $Co_2FeAl_{0.5}Si_{0.5}$ electrodes fabricated by molecular beam epitaxy, Appl. Phys. Lett. **94**, 162504 (2009).

[16] M. Yamamoto, T. Ishikawa, T. Taira, G. Li, K. Matsuda, and T. Uemura, Effect of defects in Heusler alloy thin films on spin-dependent tunnelling characteristics of $Co_2MnSi/MgO/Co_2MnSi$ and $Co_2MnGe/MgO/Co_2MnGe$ magnetic tunnel junctions, J. Phys. Condens. Matter **22**, 164212 (2010).

[17] W. H. Wang, H. Sukegawa, R. Shan, S. Mitani, and K. Inomata, Giant tunneling magnetoresistance up to 330% at room temperature in sputter deposited $Co_2FeAl/MgO/CoFe$ magnetic tunnel junctions, Appl. Phys. Lett. **95**, 182502 (2009).

[18] W. H. Wang, E. Liu, M. Kodzuka, H. Sukegawa, M. Wojcik, E. Jedryka, G. H. Wu, K. Inomata, S. Mitani, and K. Hono, Coherent tunneling and giant tunneling magnetoresistance in $Co_2FeAl/MgO/CoFe$ magnetic tunneling junctions, Phys. Rev. B **81**, 140402(R) (2010).

[19] W. H. Wang, H. Sukegawa, and K. Inomata, Temperature dependence of tunneling magnetoresistance in epitaxial magnetic tunnel junctions using a Co_2FeAl Heusler alloy electrode, Phys. Rev. B **82**, 092402 (2010).

[20] Z. C. Wen, H. Sukegawa, S. Mitani, and K. Inomata, Tunnel magnetoresistance in textured $Co_2FeAl/MgO/CoFe$ magnetic tunnel junctions on a Si/SiO_2 amorphous substrate, Appl. Phys. Lett. **98**, 192505 (2011).

[21] H. Liu, Y. Honda, T. Taira, K. Matsuda, M. Arita, T. Uemura, and M. Yamamotoa, Giant tunneling magnetoresistance in epitaxial $Co_2MnSi/MgO/Co_2MnSi$ magnetic tunnel junctions by half-metallicity of Co_2MnSi and coherent tunneling, Appl. Phys. Lett. **101**, 132418 (2012).

[22] S. Wurmehl, G. H. Fecher, K. Kroth, F. Kronast, H. A. Dürr, Y. Takeda, Y. Saitoh, K. Kobayashi, H.-J. Lin, G. Schönhense, and C. Felser, Electronic structure and spectroscopy of the quaternary Heusler alloy $Co_2Cr_{1-x}Fe_xAl$, J. Phys. D **39**, 803 (2006).

[23] S. Mizukami, D. Watanabe, M. Oogane, Y. Ando, Y. Miura, M. Shirai, and T. Miyazaki, Low damping constant for Co_2FeAl Heusler alloy films and its correlation with density of states, J. Appl. Phys. **105**, 07D306 (2009).

[24] R. Y. Umetsu, A. Okubo, and R. Kainuma, Magnetic and chemical order-disorder transformations in $Co_2Fe(Ga_{1-x}Si_x)$ and $Co_2Fe(Al_{1-y}Si_y)$ Heusler alloys, J. Appl. Phys. **111**, 073909 (2012).

[25] Y. Miura, K. Nagao, and M. Shirai, Atomic disorder effects on half-metallicity of the full-Heusler alloys $Co_2(Cr_{1-x}Fe_x)Al$: A first-principles study, Phys. Rev. B **69**, 144413 (2004).

[26] H. Sukegawa, Z. C. Wen, K. Kondou, S. Kasai, S. Mitani, and K. Inomata, Spin-transfer switching in full-Heusler Co_2FeAl-based magnetic tunnel junctions, Appl. Phys. Lett. **100**, 182403 (2012).

[27] H. Sukegawa, S. Kasai, T. Furubayashi, S. Mitani, and K. Inomata, Spin-transfer switching in an epitaxial spin-valve nanopillar with a full-Heusler $Co_2FeAl_{0.5}Si_{0.5}$ alloy, Appl. Phys. Lett. **96**, 042508 (2010).

[28] D. C. Worledge and P. L. Trouilloud, Magnetoresistance measurement of unpatterned magnetic tunnel junction wafers by current-in-plane tunneling, Appl. Phys. Lett. **83**, 84 (2003).

[29] S. Okamura, A. Miyazaki, N. Tezuka, S. Sugimoto, and K. Inomata, Epitaxial growth of ordered $Co_2(Cr_{1-x}Fe_x)Al$ full-Heusler alloy films on single crystal. substrates, Mater. Trans. **47**, 15 (2006).

[30] J. L. Vassent, M. Dynna, A. Marty, B. Gilles, and G. Patrat, A study of growth and the relaxation of elastic strain in MgO on Fe(001), J. Appl. Phys. **80**, 5727 (1996).

[31] S. Yuasa, T. Nagahama, A. Fukushima, Y. Suzuki, and K. Ando, Giant room-temperature magnetoresistance in single-crystal Fe/MgO/Fe magnetic tunnel junctions, Nat. Mater. **3**, 868 (2004).

[32] T. Ishikawa, S. Hakamata, K. Matsuda, T. Uemura, and M. Yamamoto, Fabrication of fully epitaxial $Co_2MnSi/MgO/Co_2MnSi$ magnetic tunnel junctions, J. Appl. Phys. **103**, 07A919 (2008).

[33] T. Marukame, T. Ishikawa, T. Taira, K. Matsuda, T. Uemura, and M. Yamamoto, Giant oscillations in spin-dependent tunneling resistances as a function of barrier thickness in fully epitaxial magnetic tunnel junctions with a MgO barrier, Phys. Rev. B **81**, 134432 (2010).

[34] D. D. Djayaprawira, K. Tsunekawa, M. Nagai, H. Maehara, S. Yamagata, N. Watanabe, S. Yuasa, Y. Suzuki, and K. Ando, 230% room-temperature magnetoresistance in CoFeB/MgO/CoFeB magnetic tunnel junctions, Appl. Phys. Lett. **86**, 092502 (2005).

[35] K. Tsunekawa, D. D. Djayaprawira, M. Nagai, H. Maehara, S. Yamagata, N. Watanabe, S. Yuasa, Y. Suzuki, and K. Ando, Giant tunneling magnetoresistance effect in low-resistance CoFeB/MgO(001)/CoFeB magnetic tunnel junctions for read-head applications, Appl. Phys. Lett. **87**, 072503 (2005).

[36] J. Hayakawa, S. Ikeda, F. Matsukura, H. Takahashi, and H. Ohno, Dependence of giant tunnel magnetoresistance of sputtered CoFeB/MgO/CoFeB magnetic tunnel junctions on MgO barrier thickness and annealing temperature, Jpn. J. Appl. Phys. **44**, L587 (2005).

[37] H. Sukegawa, W. H. Wang, R. Shan, and K. Inomata, Tunnel magnetoresistance in full-Heusler $Co_2FeAl_{0.5}Si_{0.5}$-based magnetic tunnel junctions, J. Magn. Soc. Jpn. **33**, 256 (2009).

[38] H. Kurt, K. Oguz, T. Niizeki, and J. M. D. Coey, Giant tunneling magnetoresistance with electron beam evaporated MgO barrier and CoFeB electrodes, J. Appl. Phys. **107**, 083920 (2010).

[39] R. H. Koch, J. A. Katine, and J. Z. Sun, Time-resolved reversal of spin-transfer switching in a nanomagnet, Phys. Rev. Lett.. **92**, 088302 (2004).

[40] Z. Li and S. Zhang, Thermally assisted magnetization reversal in the presence of a spin-transfer torque, Phys. Rev. B **69**, 134416 (2004).

[41] T. Taniguchi and H. Imamura, Dependence of spin torque switching probability on electric current, J. Nanosci. Nanotechnol. **12**, 7520 (2012); Theoretical study on dependence of thermal switching time of synthetic free layer on coupling field, J. Appl. Phys. **111**, 07C901 (2012).

[42] N. Toda, K. Saito, K. Ohta, H. Maekawa, M. Mizuguchi, M. Shiraishi, and Y. Suzuki, Highly sensitive ferromagnetic resonance measurements using coplanar waveguides, J. Magn. Soc. Jpn. **31**, 435 (2007).

[43] Z. Diao, D. Apalkov, M. Pakala, Y. Ding, A. Panchula, and Y. Huai, Spin transfer switching and spin polarization in magnetic tunnel junctions with MgO and AlO_x barriers, Appl. Phys. Lett. **87**, 232502 (2005).

[44] H. Kubota, A. Fukushima, Y. Ootani, S. Yuasa, K. Ando, H. Maehara, K. Tsunekawa, D. D. Djayaprawira, N. Watanabe, and Y. Suzuki, Evaluation of spin-transfer switching in CoFeB/MgO/CoFeB magnetic tunnel junctions, Jpn. J. Appl. Phys. **44**, L1237 (2005).

[45] J. Z. Sun, Spin-current interaction with a monodomain magnetic body: A model study, Phys. Rev. B **62**, 570 (2000).

[46] J. C. Slonczewski, Currents, torques, and polarization factors in magnetic tunnel junctions, Phys. Rev. B **71**, 024411 (2005).

[47] Y. Cui, B. Khodadadi, S. Schafer, T. Mewes, J. Lu, and Stuart A. Wolf, Interfacial perpendicular magnetic anisotropy and damping parameter in ultrathin Co_2FeAl films, Appl. Phys. Lett. **102**, 162403 (2013).

[48] H. Meng, R. Sbiaa, S. Lua, C. Wang, M. Akhtar, S. K. Wong, P. Luo, C. Carlberg, and K. S. A. Ang, Low current density induced spin-transfer torque switching in CoFeB–MgO magnetic tunnel junctions with perpendicular anisotropy, J. Phys. D **44**, 405001 (2011).

[49] W. Kim *et al.*, Extended scalability of perpendicular STT-MRAM towards sub-20nm MTJ node, IEDM Tech. Dig. 24.1.1 (2011) [http://ieeexplore.ieee.org/xpl/articleDetails.jsp?arnumber=6131602].

[50] M. T. Rahman *et al.*, Reduction of switching current density in perpendicular magnetic tunnel junctions by tuning the anisotropy of the CoFeB free layer, J. Appl. Phys. **111**, 07C907 (2012).

[51] M. Gajek *et al.*, Spin torque switching of 20 nm magnetic tunnel junctions with perpendicular anisotropy, Appl. Phys. Lett. **100**, 132408 (2012).

[52] L. Thomas *et al.*, Perpendicular spin transfer torque magnetic random access memories with high spin torque efficiency and thermal stability for embedded applications (invited), J. Appl. Phys. **115**, 172615 (2014).

[53] H. Sato, M. Yamanouchi, S. Ikeda, S. Fukami, F. Matsukura, and H. Ohno, MgO/CoFeB/Ta/CoFeB/MgO recording structure in magnetic tunnel junctions with perpendicular easy axis, IEEE Trans. Magn. **49**, 4437 (2013).

[54] Z. C. Wen, H. Sukegawa, S. Kasai, M. Hayashi, S. Mitani, and K. Inomata, Magnetic tunnel junctions with perpendicular anisotropy using a Co_2FeAl full-Heusler alloy, Appl. Phys. Express **5**, 063003 (2012).

[55] K. Chae, D. Lee, T. Shim, J. Hong, and J. Park, Correlation of the structural properties of a Pt seed layer with the perpendicular magnetic anisotropy features of full Heusler-based $Co_2FeAl/MgO/Co_2Fe_6B_2$ junctions via a 12-inch scale Si wafer process, Appl. Phys. Lett. **103**, 162409 (2013).

[56] M. S. Gabor, T. Petrisor, Jr., C. Tiusan, and T. Petrisor, Perpendicular magnetic anisotropy in $Ta/Co_2FeAl/MgO$ multilayers, J. Appl. Phys. **114**, 063905 (2013).